ARTICLE

Directed Block Copolymer Assembly *versus* Electron Beam Lithography for Bit-Patterned Media with Areal Density of 1 Terabit/inch^2 and Beyond

XiaoMin Yang,[†,*] Lei Wan,[†] Shuaigang Xiao,[†] Yuan Xu,[†] and Dieter K. Weller[‡]

[†]Seagate Research Center, 1251 Waterfront Place, Pittsburgh, Pennsylvania 15222, and [‡]Seagate Media Research, 47010 Kato Road, Fremont, California 94538

ABSTRACT The directed self-assembly of block copolymer (BCP) offers a new route to perfect nanolithographic patterning at sub-50 nm length scale with molecular scale precision. We have explored the feasibility of using the BCP approach *versus* the conventional electron beam (e-beam) lithography to create highly dense dot patterns for bit-patterned media (BPM) applications. Cylinder-forming poly(styrene-*b*-methyl methacrylate) (PS-*b*-PMMA) directly self-assembled on a chemically prepatterned substrate. The nearly perfect hexagonal arrays of perpendicularly oriented cylindrical pores at a density of approximately 1 Terabit per square inch (Tb/in.^{2}) are achieved over an arbitrarily large area. Considerable gains in the BCP process are observed relative to the conventional e-beam lithography in terms of the dot size variation, the placement accuracy, the pattern uniformity, and the exposure latitude. The maximum dimensional latitude in the cylinder-forming BCP patterns and the maximum skew angle that the BCP can tolerate have been investigated for the first time. The dimensional latitude restricts the formation of more than one lattice configuration in certain ranges. More defects in BCP patterns are observed when using low molecular weight BCP materials or on non-hexagonal prepatterns due to the dimensional latitude restriction. Finally, the limitations and challenges in the BCP approach that are associated with BPM applications will be briefly discussed.

KEYWORDS: directed self-assembly · block copolymers · lithography · bit-patterned media · magnetic recording

*Address correspondence to xiaomin.yang@seagate.com.

Received for review January 23, 2009 and accepted June 18, 2009.

Published online July 2, 2009.
10.1021/nn900073r CCC: $40.75

Bit-patterned media (BPM) is one of the advanced technologies that are currently being considered, for the near future, to satisfy the ever-increasing demand for higher storage capacity in the magnetic recording industry.[1,2] However, BPM presents extreme challenges to lithography because of the small feature sizes and the tight spacing tolerances needed to achieve high-density recording. For instance, for a reasonable signal-to-noise ratio (SNR), the bit size and bit positioning variation should not exceed approximately 5% for a staggered media design at the density of 1 Tb/in.^{2} based on the results from computer modeling predictions.[3] Today neither optical nor EUV lithography is capable of reaching these dimensions and economics. In other words, BPM requires more aggressive lithography targets than the semiconductor industry, and the latter will not provide a lithography solution in time for BPM applications based on the ITRS roadmap.[4] However, compared to the semiconductor industry, BPM has the advantage of only requiring a single mask step with no critical layer-to-layer alignment involved. Electron beam (e-beam) direct writing combined with nanoimprint lithography (NIL) is currently considered to be the only choice for this application.[5,6] In this approach, the e-beam lithography is employed to fabricate a "perfect" master template while the imprint process provides the high throughput patterning. The imprinted patterns are then transferred into disks by using either a subtractive process (etch or ion milling) or an additive process (plating or deposition), thus forming periodic arrays of isolated magnetic islands. Besides the requirements for very precise imprinting and pattern transfer on the sub-25 nm scale, high throughput and manageable costs are also critical for this technology to be of value to manufacturing.

Currently, e-beam lithography sets the resolution stage for template mastering. High-resolution dot patterning for BPM applications has been previously demonstrated up to ~4.5 Tb/in.^{2} by using direct e-beam writing with nonchemically amplified resist; however, the writing area is typically only a small portion of the disk.[7] It still remains very challenging to achieve defect-free quality over a full disk-size area by only using the conventional e-beam lithography. One of the practical issues is the extremely long writing time associated with the e-beam series-writing scheme. For example, using high-resolution ZEP520 e-beam resist, it would take several weeks

to write a 2.5 in. disk-sized template at the pattern density of 1 Tb/in.^{2}. This writing time is significantly longer than a viable commercial process can tolerate. A practical lithographical solution for BPM applications is urgently needed therefore. One promising approach to overcome the conventional e-beam lithographic limitations is to combine e-beam lithography with self-assembly materials, such as diblock copolymers. In this approach, e-beam lithography techniques are used to create prepatterned surfaces, either a chemically patterned surface[8−10] or topographically patterned surface,[11−13] that manipulate the wetting behavior of block copolymer films and guide the block copolymer into self-assembled domains at the length scale of 5−50 nm with molecular scale precision.[14,15] In this paper, we only focus our study on the chemical prepattern approach for BPM applications because this approach can provide both long-range ordering and feature registration. The concept of this approach and some preliminary results of using a prepatterned monolayer surface with different chemical contrast to direct the long-range order in a symmetric diblock copolymer film were demonstrated earlier.[8,16,17] Since that time, the BCP pattern quality has been greatly improved by using an improved prepatterning process.[9,10] Very recently, it was shown that this approach could significantly improve the e-beam patterning quality especially at high density and also enhance the pattern pitch resolution by a factor of at least 2.[18−20] Since the self-assembly BCP process is driven by thermodynamic driving forces, people have experimentally demonstrated several major advantages over the conventional e-beam lithographic process that is driven by kinetic driving forces. The first advantage is called "pattern rectification" that improves the e-beam pattern quality especially at high density, such as line or dot roughness, pattern uniformity, *etc*. The second is called a "self-healing" effect that repairs the defects, such as the missing dots, thus reducing the defect density in the e-beam lithography. The third is called "pattern interpolation" or "density multiplication" that enhances the dense feature pitch resolution by a factor of at least 2, thus increasing the pattern density by a factor of at least 4. The patterning scheme of density multiplication can significantly reduce the e-beam writing time since the e-beam only needs to write every fourth dot, and the BCP domains will fill in the other corresponding three dots.

The purpose of this work is to further explore the BCP approach to see if it is really suitable for BPM applications. This includes understanding its advantages and the limitations associated with BPM design space. We performed the detailed experimental study for this purpose. Cylinder-forming P(S-*b*-MMA)s with three different molecular weights were used as the BCP system for this study. The P(S-*b*-MMA) directly self-assembles on a chemically prepatterned PS brush substrate to form the highly ordered cylindrical pores at a pattern density of approximately 1 Tb/in.^{2} over a large area. A systematic study has been carefully conducted to compare the BCP process to the conventional e-beam process in terms of feature size distribution, placement accuracy, pattern uniformity, and the process latitude. Also, the following aspects associated with the understanding of the BCP capabilities for BPM applications were studied in this paper: (1) the incommensurability between surface pattern dimension and BCP nature dimension to understand the maximum dimensional latitude that the BCP pattern can either stretch or compress to; (2) the skewed hexagonal prepattern study to understand the maximum skew angle that the BCP pattern can follow and still maintain long-range ordering; (3) the BCP pattern quality of low molecular weight cylinder-forming P(S-*b*-MMA) to push pattern density; and (4) the effect of having a non-hexagonal prepattern in the substrate on BCP pattern quality. Some of the possible solutions to potentially overcome these limitations will also be discussed in the present work.

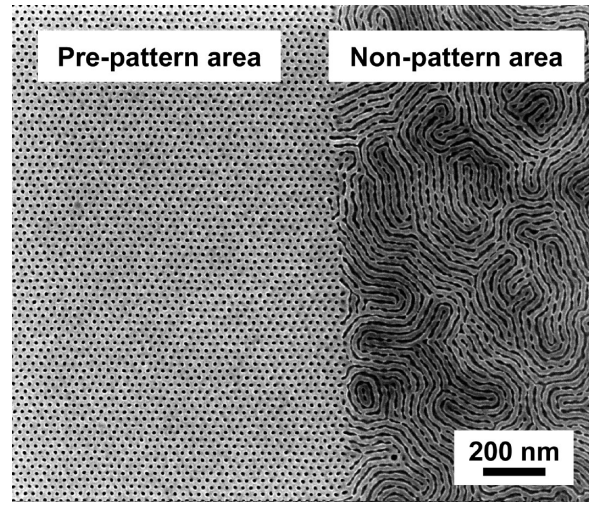

Figure 1. SEM image of P(S-*b*-MMA) (L_0= 28.6 nm) film on a partially prepatterned substrate. The left side is the prepatterned area by e-beam lithography with a surface pattern pitch L_s = 28 nm, whereas the right side is a non-prepatterned area.

RESULTS AND DISCUSSION

Pattern Quality Improvement and Exposure Latitude Increase. Nearly perfect long-range ordering in the self-assembled P(S-*b*-MMA) thin film can be achieved by using a chemically prepatterned substrate when the surface pattern periodicity L_s is equal (or close) to the BCP bulk equilibrium periodicity L_0. Figure 1 shows a top-down SEM image of a 45 nm thick (~1.6L_0) P(S-*b*-MMA) film with L_0 = 28.6 nm on a partially prepatterned substrate. The left side in Figure 1 is the prepatterned area that has a hexagonal prepattern with a surface pattern pitch L_s = 28 nm created by e-beam lithography, whereas the right side in Figure 1 is a non-prepatterned area for the purpose of showing the difference of the BCP behavior on these two areas. The left side clearly shows a highly ordered dense dot pattern with good

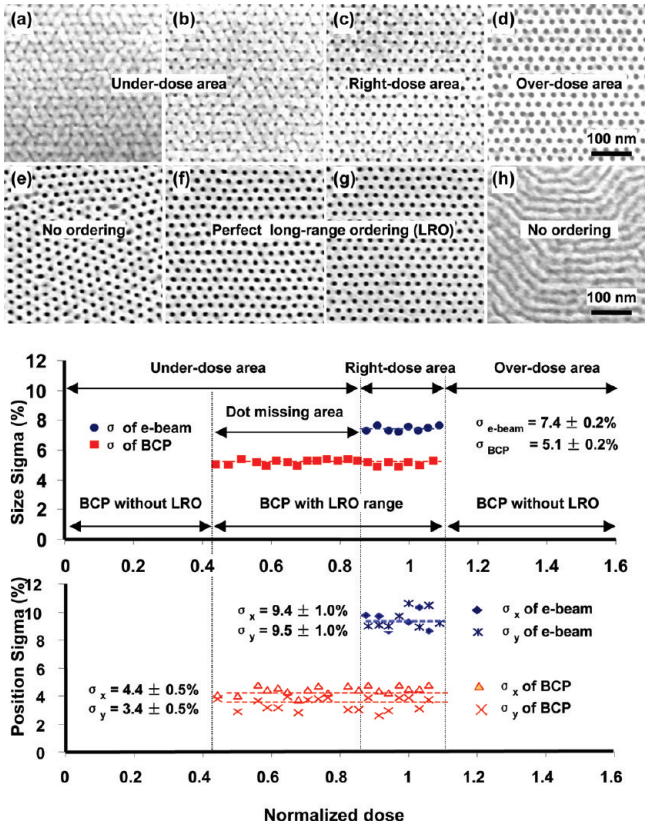

Figure 2. (a−d) SEM images of the e-beam resist pattern (L_s = 28 nm) exposed at doses of 30, 44, 66, and 86 mC/cm^2, respectively. (e−h) SEM images of P(S-*b*-MMA) (L_0 = 28.6 nm) patterns on prepatterns resulting from the corresponding e-beam resist patterns above. The size σ (upper graph) and position σ (lower graph) of e-beam resist pattern (in blue) and directed P(S-*b*-MMA) patterns (in red) as a function of normalized e-beam exposure dose. The actual e-beam exposure dose = 68 mJ/cm^2 × normalized dose.

registration to the underneath surface prepatterns and with long-range ordering over the entire prepatterned area, but the right side shows random BCP domains in the BCP films. The dark dense dots on the prepatterned area are cylindrical pores, which are standing upright with the PMMA block removed and only the PS block matrix remaining. To the contrary, the cylindrical PMMA block domains on the non-prepatterned area are lying down, forming random domain structures in the BCP films. The highly ordered dense features in the BCP films could possibly be used as self-assembling resist materials to create a template for BPM applications. However, it should be emphasized that the BPM specification does not only require the small feature size but also requires the narrow size distribution and tight center-to-center spacing. Precise placement of the individual dots and the size uniformity are two key factors that certainly affect the performance of patterned media in magnetic recording. Therefore, it would be important to further compare the size distribution and the position accuracy between the self-assembled process and the conventional e-beam lithographic process to see how large any additional benefits will be from the BCP process. A systematic experimental study has been carefully performed for this purpose. Figure 2 summarizes the experimental results. The size and position σ is plotted as a function of e-beam normalized dose (the actual e-beam exposure dose = 68 mJ/cm^2 × normalized dose). Figure 2a−d shows top-down SEM images of the developed ZEP520 resist patterns, which were exposed at doses of 30, 44, 66, and 86 mC/cm^2, respectively. The resist patterns are hexagonal dot arrays with a pattern pitch of L_s = 28 nm, and they are used to create chemical prepatterns for guiding the self-assembly of P(S-*b*-MMA) with a L_0 = 28.6 nm. The corresponding BCP patterns with a pattern pitch of L_p = 28 nm (corresponding to a pattern density of 950 Gigabits per square inch, Gb/in.^{2}) are shown in Figure 2e−h. E-beam patterning only in the dose range of 60−72 mC/cm^2 shows well-defined ZEP520 patterns with a size variation of 7.4 ± 0.2%, as shown in the upper graph of Figure 2. These size variation values are repeatable from our routine e-beam process using the VB6 e-beam tool operated at 100 kV. In contrast to the size variation from the e-beam patterning process, the self-assembled BCP cylindrical pores show a better pattern quality with a reduced size variation of 5.1 ± 0.4%. It is speculated that the molecular weight distribution and the interface width between the PS block and PMMA block determine size uniformity. A similar trend has been observed from the results of the pattern placement accuracy analysis as well, as shown in the lower graph of Figure 2. E-beam patterning gives a pattern placement accuracy of 9.4 ± 1.0% along the *x*-direction and 9.5 ± 1.0% along the *y*-direction; in contrast, the self-assembled BCP gives a pattern placement accuracy of 4.4 ± 1.0% along the *x*-direction and 3.4 ± 1.0% along the *y*-direction. Again, a significant improvement is also seen in the pattern placement accuracy. It should be mentioned that the σ values of the size variation and placement accuracy of the ZEP520 resist patterns were not given in the e-beam exposure dose range of <60 mC/cm^2 because there were some dots missing in the resist patterns due to the under-dose effect. Similarly, the σ values of both patterns were not measured at the dose range in which the BCP patterns did not show any long-range ordering, such as <30 mC/cm^2 (much under-dose range) or >72 mC/cm^2 (over-dose range).

Not only is there a significant benefit from both the size distribution and the positioning accuracy, but also the BCP process shows wider exposure latitude. With the conventional e-beam patterning process, as the pitch gets progressively smaller, the energy contrast between the exposed and unexposed areas goes down quickly, making it more difficult to form high-resolution dot patterns in the latent image and developed resist.[7] Thus, it is difficult to obtain a high-quality e-beam pattern over a large area, especially when the dot pitch is less than 25 nm, as is required to achieve a pattern density of 1 Tb/in.^{2} and above. In general, the e-beam li-

thography has a narrow exposure latitude and small process window for highly dense feature patterning. Any minor changes in the process conditions, such as beam focus drift, beam noise and stability, developer temperature drift, *etc.*, could badly degrade the e-beam pattern quality. In the present experiment, the ZEP520 dense dot patterns appear under-dosed when the exposure dose is lower than approximately 60 mC/cm^2, showing undersized dots with some dots not being fully opened (Figure 2a,b). As the dose goes above 72 mC/cm^2, the ZEP520 patterns show the oversized dots with some connected to each other (Figure 2d). It was found that the right dose for ZEP520 dot patterns under the present experimental conditions is in the range of 60−72 mC/cm^2 for a given exposed area of 1 mm × 3 mm. In contrast, the nearly perfect ordered cylindrical pores in the P(S-*b*-MMA) film can be achieved on a prepatterned surface that was exposed with a dose range of 30−72 mC/cm^2. The dose range for the BCP process is approximately four times wider than that of the e-beam dose range. The reason why the BCP process still works at a lower dose range is because the O_2 RIE process, after e-beam patterning, can still etch away the resist residue, in the bottom of the pore, along with the 2−3 nm thick PS brush layer to expose the underlying SiO_x surface to form the chemical prepattern. The experimental results indicate that the chemical prepatterns are used as a guidepost only and they do not necessarily need to be perfect in pattern quality. The BCP process can tolerate certain defects existing in the prepatterns, such as under dosed dots, missing dots, or connected dots. Obviously, if the e-beam exposure dose is too low during the e-beam patterning, then the O_2 RIE process cannot clear the extra resist residue from all of the pores, and thus no chemical prepattern can be formed on the substrate. Similarly, when the exposure dose is too high, then no chemical prepatterns will be formed because the e-beam patterns are vastly oversized and the O_2 RIE process causes the entire surface to become chemically homogeneous. It is noticed that the hole size in the ZEP520 resist pattern increases a little bit with the increasing exposure dose, resulting in an increase in the exposed SiO_x dot diameter. However, the size of the cylindrical pores remains constant in the cylinder-forming P(S-*b*-MMA) film because the domain size is dependent on the molecular weight and the composition of the BCP blocks, not the exposure dose of the e-beam pattern. Similar results have been demonstrated in both the experiment and the simulation work for the lamella-forming P(S-*b*-MMA),[21] which can form perfect patterns on chemical prepatterns having ratios of the PS-philic stripe width/L_s between 0.36 and 0.63. Approximately 30% volume fraction of PMMA block in P(S-*b*-MMA) films results in a PS matrix with pores having a diameter of approximately 0.55L_0. The lower the molecular weight, the smaller the pore size will be. Also, low purity and high polydispersity of the BCP material can introduce more defects in the BCP film.[22,23]

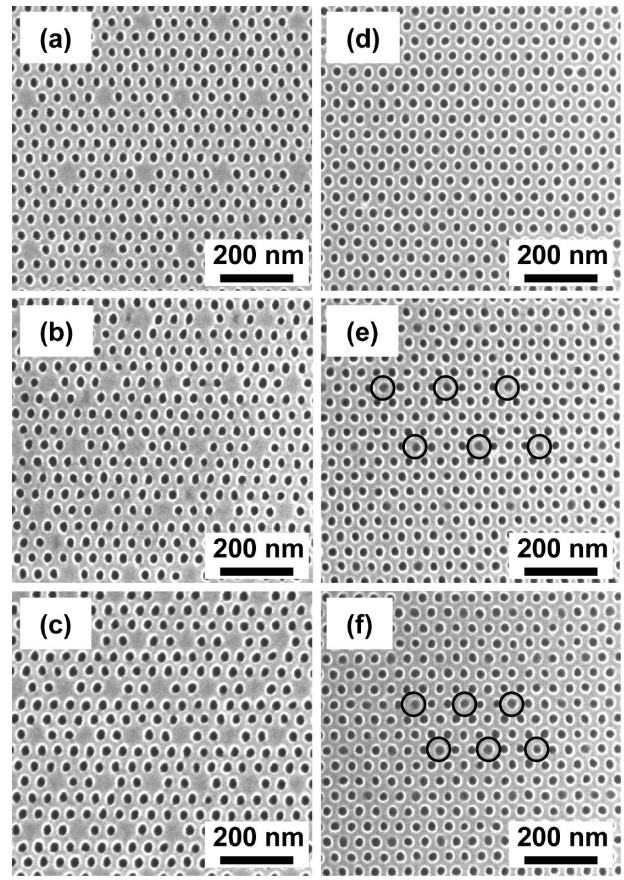

Figure 3. SEM images of the e-beam resist patterns (L_s = 42 nm) with one individual dot purposely left out of every (a) 5 × 5 array, (b) 4 × 4 array, and (c) 3 × 3 array. (d−f) SEM images of P(S-*b*-MMA) (L_0 = 42 nm) patterns directed by the prepatterns resulting from corresponding e-beam resist patterns on the left. All the intentionally skipped spots in the e-beam prepatterns show up in the BCP patterns, as marked in circles.

Self-Healing Effect. Another major advantage of the BCP process over the conventional e-beam process is the ability to self-heal the defects existing in the prepatterns, such as missing dots, mal-formed dots, connected dots, *etc*. As an example, the SEM images in Figure 3 show that the BCP process can repair the dot missing in the e-beam prepattern. Figure 3a−c shows the e-beam resist patterns (L_s = 42 nm) with one individual dot purposely left out of every 5 × 5 array (Figure 3a), 4 × 4 array (Figure 3b), and 3 × 3 array (Figure 3c). Figure 3d−f shows the corresponding BCP patterns (L_p = 42 nm) with all dots showing up, including at the sites where the dots in the prepattern were intentionally skipped during the e-beam patterning. It is noticeable that these interpolated BCP dots sitting on the remaining substrate have a different gray tone from those BCP dots sitting on the chemically patterned spots. This slight difference in SEM image contrast (marked in Figure 3e,f) could be due to the PS brush residue remaining inside the PS cylindrical holes. As the

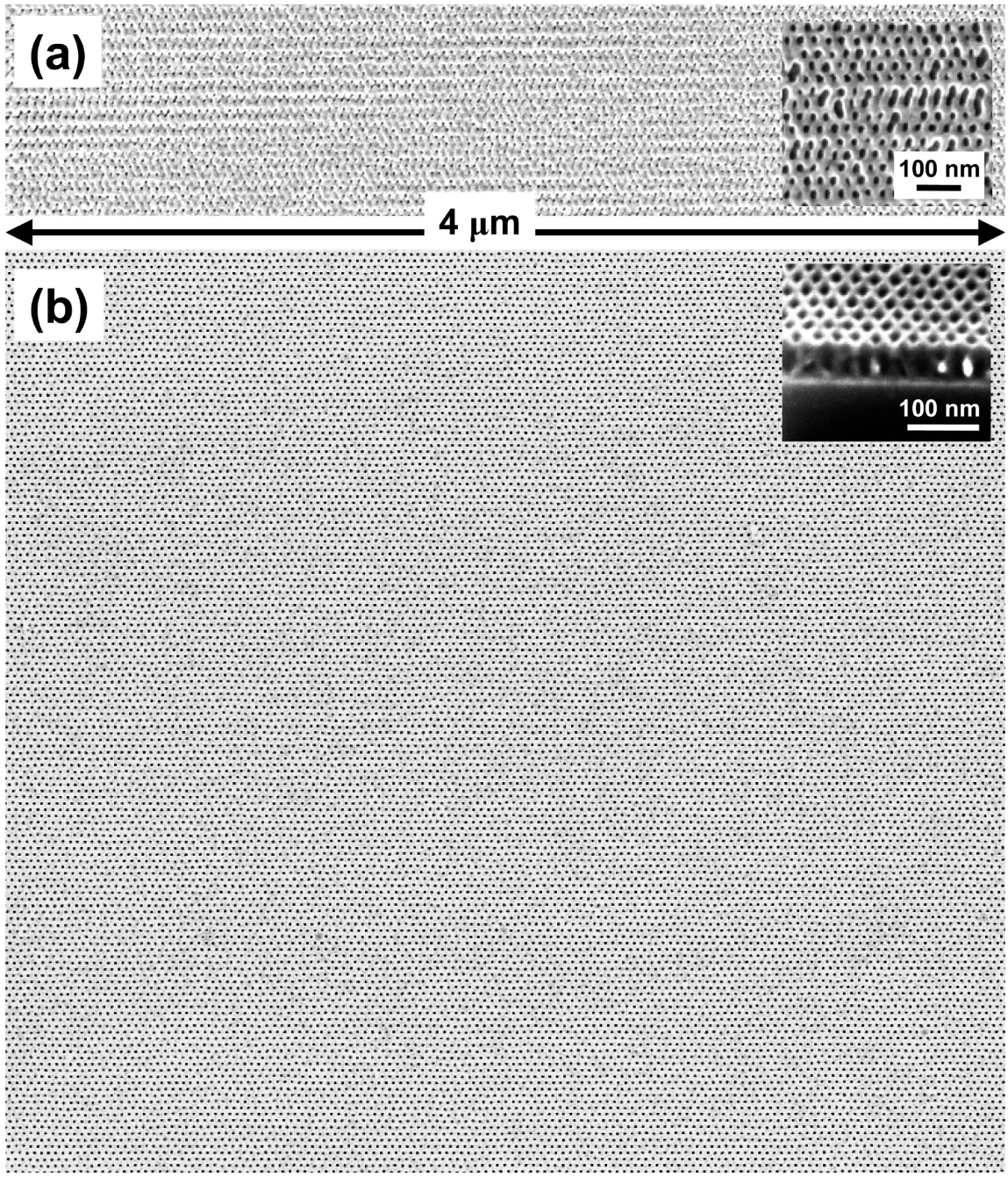

Figure 4. (a) SEM images of a low quality e-beam resist pattern (L_s = 28 nm). A magnified image is shown in the inset. (b) Large area SEM image of P(S-*b*-MMA) (L_0 = 28.6 nm) pattern resulting from the corresponding e-beam resist pattern shown in (a). The inset shows cross-sectional SEM image of the P(S-*b*-MMA) film.

density goes up to and beyond 1 Tb/in.^{2}, more defects will show up in the e-beam prepatterns, and the BCP process can rectify some of them. Thus, the chemical prepattern does not need to have the device-level quality. As another example of a poor e-beam prepattern, Figure 4a shows a SEM image of a low-quality ZEP520 resist pattern with L_s= 28 nm (950 Gb/in.^{2}). The magnified SEM image (inserted in Figure 4a) shows many connected dots that degraded the periodic structure of e-beam pattern. These low-quality resist patterns are commonly seen in high-density e-beam lithography. Surprisingly, a nearly perfect BCP pattern, as shown in Figure 4b, was obtained from the low-quality prepattern substrate shown in Figure 4a. Not only are all of the individual dots present and well-separated but also the overall pattern uniformity is much improved compared to the e-beam resist pattern in Figure 4a. The cross-sectional SEM image inset in Figure 4b shows all of the PS pores open to the substrate with reasonably vertical sidewalls. Such good quality BCP patterns were seen in all of the samples from our experiments. The defect density (dot missing or too small in size) observed

on the samples is on the order of 10^{-3} to 10^{-4} on a patterned area of 3 mm × 1 mm.

Density Multiplication for Dot Pitch Resolution Enhancement and E-Beam Writing Time Reduction. Recently, several groups have experimentally demonstrated that the pitch resolution in either dense line patterns or dot patterns can be enhanced using the BCP self-assembly proces.[18−20] The characterization of this method was called pattern interpolation or density multiplication. The basic idea is first to use the e-beam to print a prepattern (either chemical epitaxy[18,20] or graphoepitaxy[19]) with a periodicity (L_s) larger than the BCP bulk equilibrium periodicity (L_0) (lamella,[20] cylinder,[18] or sphere[19]), and then to guide the self-assembly of BCP on the prepattern with density multiplication by a factor of $(L_s/L_0)^2$. The same results have been obtained in the present experiments. A chemical prepattern with L_s = 56 nm (~$2L_0$) was prepared from e-beam patterning (Figure 5a), and then the cylinder-forming P(S-*b*-MMA) with a L_0 = 28.6 nm was coated on the prepatterned surface, which resulted in a nearly perfect BCP hexagonal pattern with a BCP pattern pitch L_p = 28 nm (Figure 5b). Clearly, a 4-fold increase in the pattern density has been demonstrated in this case since the pitch was halved in both the *x*- and *y*-directions. The long-range-ordered perpendicular BCP cylindrical pores were seen for a film thickness range from $1.0L_0$ to $1.8L_0$, whereas parallel BCP cylinders were seen when the BCP film thickness was out of this thickness range. Nearly perfect BCP patterns were present on prepatterns with a wide e-beam exposure dose range from 35 to 90 mC/cm^2. It is noticed that this dose range for L_s = 56 nm (~$2L_0$) is even wider than that of directing on chemical prepatterns with the L_s = 28 nm (~L_0) (30−72 mC/cm^2). All of these patterns showed variation values similar to those from prepatterns with L_s = 28 nm regarding both the size distribution and the placement accuracy. It was observed that there was no difference in the size of the BCP pattern between the dots sitting on the chemically patterned spots and the remaining substrate. To better investigate the three-dimensional structure of the cylindrical pores through the entire film thickness, BCP samples with a patterned area of 3 mm × 1 mm were cleaved for cross-sectional SEM imaging. Figure 5c shows a typical cross-sectional SEM image of the BCP pattern with L_p = 28 nm guided by a prepattern with L_s = 56 nm. It is not possible to tell whether the cleaved plane crosses prepatterned dots or not from a sample cleave process. However, all of the cross-sectional SEM images from several different samples show that the perpendicular BCP cylindrical pores go through the entire film thickness with a vertical sidewall profile. The aspect ratio of the BCP domains (height/diameter) is approximately 4, as shown in Figure 5c. A vertical sidewall profile in the BCP films is very desirable for BPM master template fabrication. The vertical sidewall profile in the BCP films also represents the strong interaction between the PS brush and the PS block and between patterned bare SiO_2 sites and the PMMA block based on the previous simulation results.[18,24] Here, the cylinder-forming P(S-*b*-MMA) film has an upper limit pitch multiplication factor of 2. The upper limit of the pitch multiplication factor is more than 4 for the sphere-forming P(S-*b*-DMS) film with a volume fraction of PDMS of 16.5% (L_0 = 40 nm) using PS brush or PDMS brush functionalized hydrogen silsesquioxane (HSQ) posts as topographical prepatterns.[19] Cheng *et al.* were able to

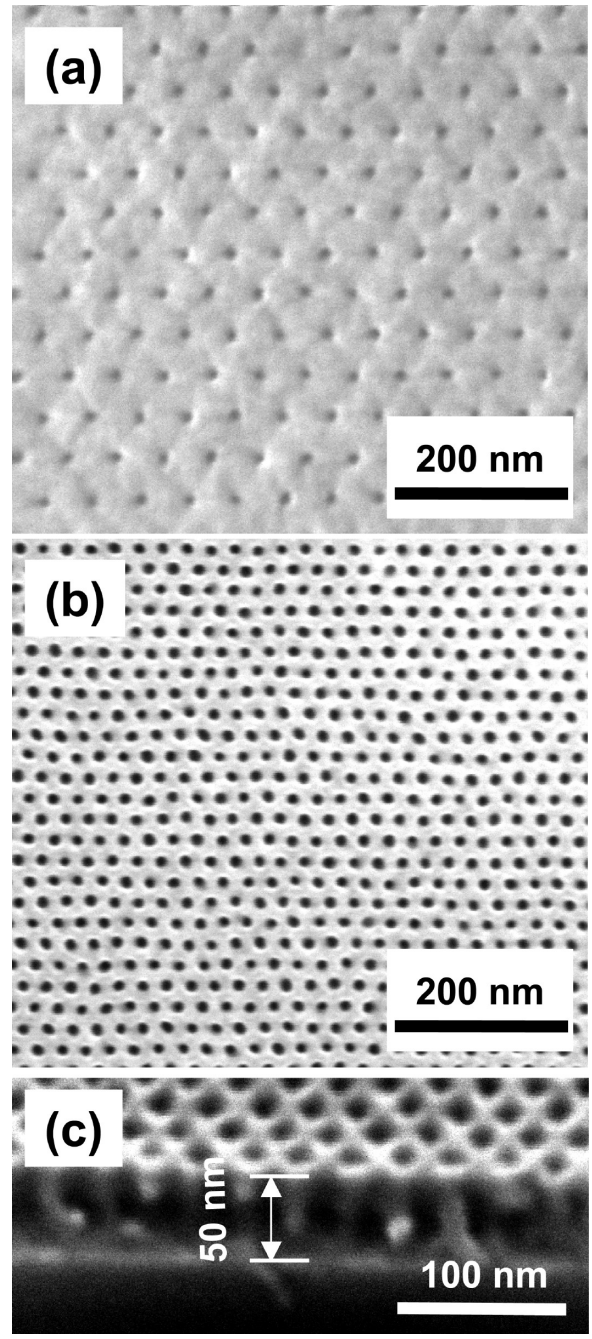

Figure 5. (a) SEM image of the e-beam resist pattern (L_s = 56 nm). (b) SEM image of P(S-*b*-MMA) ($L_p = 1/2L_s$ = 28 nm) directed by the prepattern corresponding to the e-beam resist pattern shown in (a). (c) Cross-sectional SEM image of the BCP film.

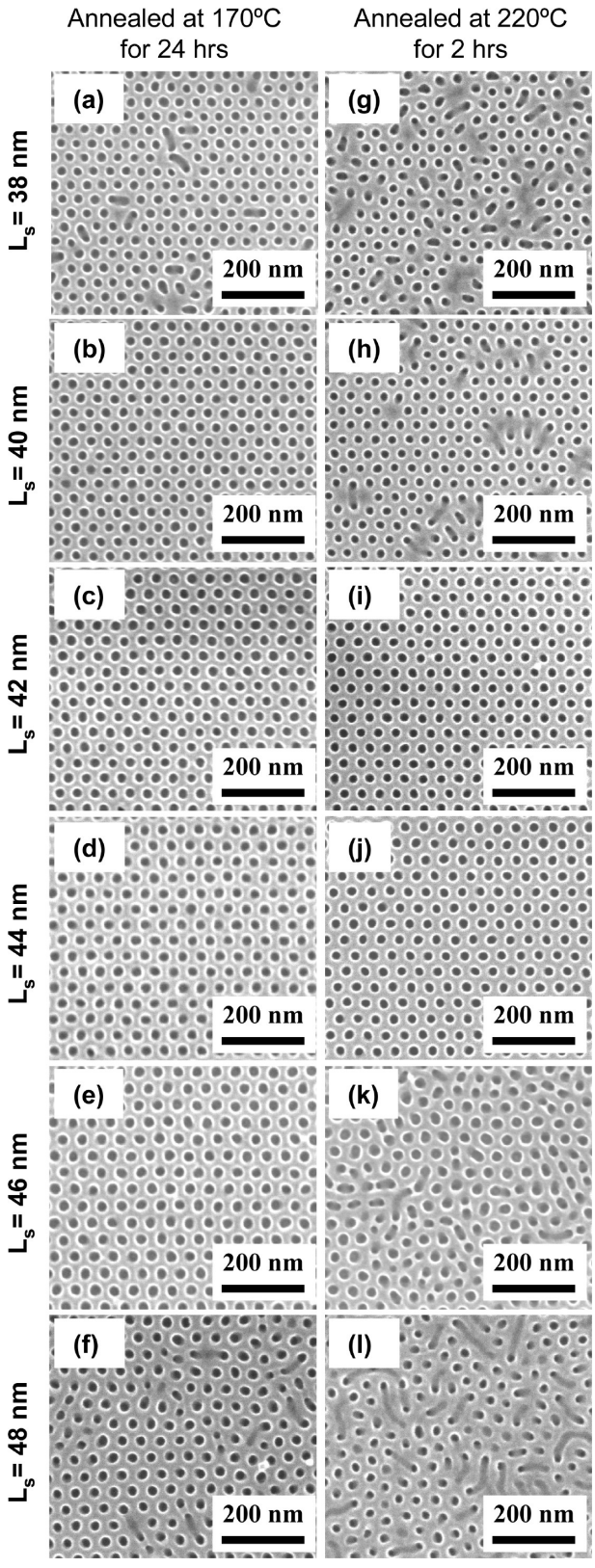

Figure 6. SEM images of P(S-*b*-MMA) (L_0 = 42 nm) patterns guided by prepatterns with L_s = 38, 40, 42, 44, 46, and 48 nm. The BCP samples were annealed either at 170 °C for 24 h (a−f) or at 220 °C for 2 h (g−l).

achieve perfect spatial frequency quadrupling for P(S-*b*-MMA) lamella at a length scale of ~1.5 μm.[20] When cylinder-forming P(S-*b*-MMA) (L_0 = 28.6 nm) is guided by chemically patterned PS brush with L_s = 87 nm (~3L_0), our preliminary results show BCP locally formed hexagonal structures with $L_p \sim L_0$ but with no long-range ordering in the film. The reason that cylinder-forming P(S-*b*-MMA) has a smaller upper limit multiplication factor than sphere-forming P(S-*b*-DMS) or lamella-forming P(S-*b*-MMA) may be due to the former having lower defect formation energy and slower kinetics. It may also be due to the non-optimized experimental conditions in which the BCP system is not reaching the possible thermodynamic equilibrium. We believe that using an improved prepattern system that has a stronger chemical affinity than the current one can further raise the upper limit of the density multiplication factor for the cylinder-forming P(S-*b*-MMA) system.

Dimensional Latitudes and Lattice Commensurability. As mentioned earlier, the self-assembly process directed by a prepattern with a periodicity of L_s equal (or close) to the BCP bulk equilibrium periodicity L_0 usually leads to highly ordered BCP patterns due to the minimum free energy in the self-assembly process.[9,25] Incommensurability between L_s and L_0 will induce various defects in the BCP patterns.[8,26] However, using a chemical prepattern with a strong affinity to the corresponding BCP blocks can stretch or compress the BCP chains and stabilize BCP films with L_p deviating from L_0 within a certain range.[25] Here the dimensional latitudes for cylinder-forming P(S-*b*-MMA)s with three different molecular weights were investigated on a chemically patterned PS brush matrix with a hexagonal hydrophilic dot array (SiO_2 sites). Figure 6 shows the top-down SEM images of the P(S-*b*-MMA) (L_0 = 42 nm) films guided by chemical prepatterns at surface pattern pitches of L_s = 38, 40, 42, 44, 46, and 48 nm. The BCP samples were annealed either at 170 °C for 24 h (Figure 6a−f) or at 220 °C for 2 h (Figure 6g−l). When the sample was annealed at 170 °C, the upright BCP cylinders were defect-free long-range-ordered and registered to the prepatterns ranging from 40 nm ≤ L_s ≤ 46 nm (Figure 6b−e). Within this dimensional range, the BCP pattern with a period of L_p can still match with the surface prepattern with a period of L_s, which represents either compression or stretching of the BCP chains. For the case of $L_s \leq$ 38 nm (Figure 6a), some short-range defects in PMMA cylindrical blocks that are connected to neighboring PMMA cylindrical blocks showed up as the results of too much compression of the BCP polymer chains. With $L_s \geq$ 48 nm (Figure 6f), the PMMA cylindrical blocks appeared to be more deformed and connected due to the over stretching of the polymer chains. As the L_s deviates from the dimensional latitude, the BCP patterns eventually lose their long-range ordering. When the BCP films were annealed at 220 °C for 2 h, the defect-free long-range ordering was achieved over a shorter surface pattern dimensional range from 42 nm ≤ L_s ≤ 44 nm (Figure 6i,j), compared to that of the samples an-

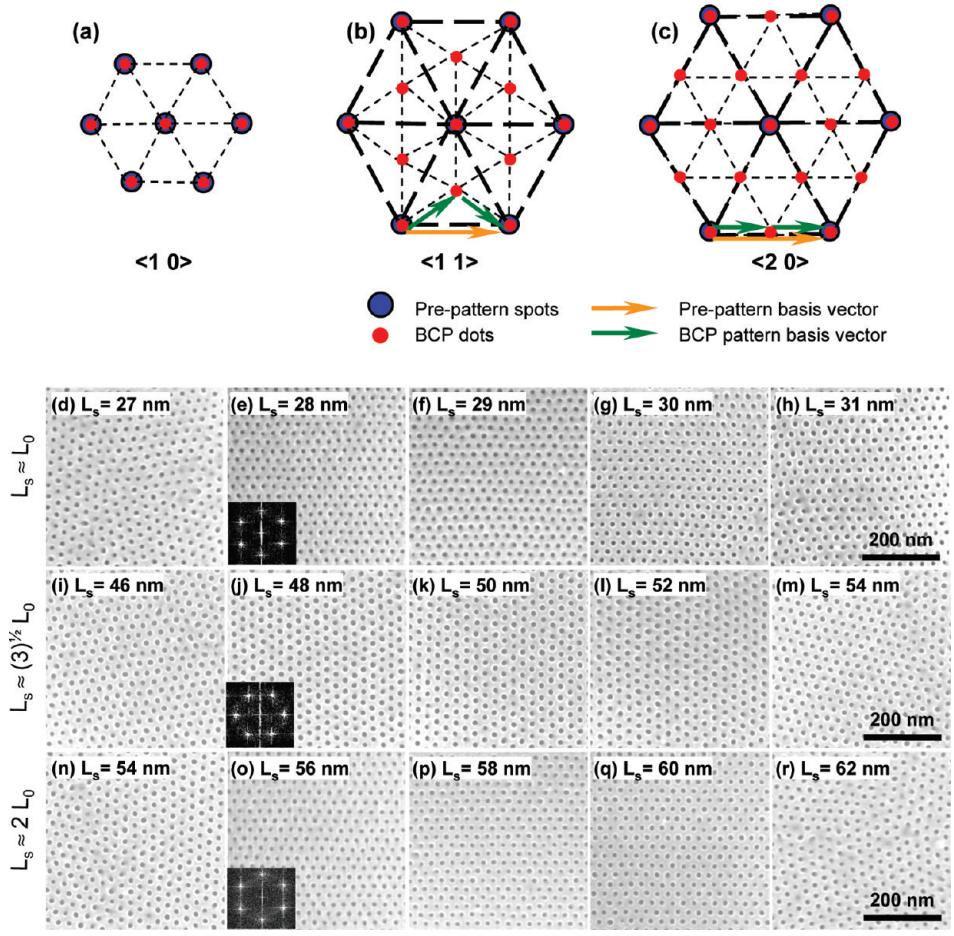

Figure 7. (a−c) Illustration of the <1 0>, <1 1>, and <2 0> BCP lattice configurations, respectively. (d−r) SEM images of P(S-*b*-MMA) patterns directed by prepatterns with various L_s values. (d−h) $L_s \approx L_0$, 27 nm ≤ L_s ≤ 31 nm, (i−m) $L_s \approx \sqrt{3}L_0$, 46 nm ≤ L_s ≤ 54 nm, and (n−r) $L_s \approx 2L_0$, 54 nm ≤ L_s ≤ 62 nm. The insets show the 2D FFT graphs.

nealed at 170 °C for 24 h. This preliminary result indicates that the maximum dimensional range the BCP can stretch or compress to is very sensitive to the thermal annealing parameters, such as annealing time and temperature. Optimizing the annealing conditions may still increase the maximum dimensional range for any given BCP system.

We further investigated the commensurability in the case when $L_s > L_0$ with consideration of combining both the dimensional range and the lattice configurations. This combined commensurability study is conducted here using a cylinder-forming P(S-*b*-MMA) with a L_0 = 28.6 nm. When L_s is equal (or close) to L_0, the PMMA cylinders in the BCP films will precisely register on each prepatterned spot and appear to be a <1 0> lattice configuration (Figure 7a). As L_s is increased to (or close to) $\sqrt{3}L_0$, then a <1 1> BCP lattice configuration will be commensurate to the prepattern lattice with a 30° rotation relative to the <1 0> direction (Figure 7b). Two equal length basis vectors of the BCP lattice (green arrows as shown in Figure 7b) add up and form one prepattern basis vector (yellow arrow as shown in Figure 7b). With a continuous increase in the surface pattern pitch $L_s \sim 2L_0$, a <2 0> BCP lattice configuration will

TABLE 1. Calculated L_p of Possible P(S-*b*-MMA) (L_0 = 28.6 nm) Patterns Guided by Prepatterns with 46 nm (1.6L_0) ≤ L_s ≤ 62 nm (2.2L_0) with Different Lattice Configurations and Experimental Results of Lattice Configurations and L_p

L_s (nm)	46	48	50	52	54	56	58	60	62
<1 1> L_p (nm)	26.6	27.7	28.9	30.0	31.2	32.3	33.5	34.6	35.8
<2 0> L_p (nm)	23.0	24.0	25.0	26.0	27.0	28.0	29.0	30.0	31.0
<2 1> L_p (nm)	17.3	18.1	18.9	19.7	20.4	21.2	21.9	22.7	23.4
Lattice config.	N/A	<1 1>	<1 1>	<1 1>	N/A	<2 0>	<2 0>	<2 0>	N/A
Experim. L_p (nm)	28.6	27.8	29.0	29.5	28.7	28.1	29.0	29.6	28.6

form in the BCP film (Figure 7c). In this case, the BCP lattice basis vector (green arrows as shown in Figure 7c) is parallel to prepattern basis vector (yellow arrows as shown in Figure 7c) but is half of the prepattern length. A group of top-down SEM images shown in Figure 7d−r were taken from a P(S-*b*-MMA) film with L_0 of ~28.6 nm, but on prepatterns with three different pitches ranging from (1) $L_s \approx L_0$, 27 nm $\leq L_s \leq$ 31 nm (Figure 7d−h); (2) $L_s \approx \sqrt{3}L_0$, 46 nm $\leq L_s \leq$ 54 nm (Figure 7i−m); and (3) $L_s \approx 2L_0$, 54 nm $\leq L_s \leq$ 62 nm (Figure 7n−r). For the case of $L_s \approx L_0$ (Figure 7d−h), perfect PMMA cylinders with <1 0> lattice configuration can be obtained for both $L_s = 28$ and 29 nm and nearly perfect structures for $L_s = 30$ nm. When $L_s \leq 27$ nm, the prepattern failed to induce the compression of the BCP chains. Similarly, the prepattern could not induce the stretching of the BCP chains when $L_s \geq 31$ nm. In both cases, the BCP pattern locally formed hexagonal structures with the pattern periodicity close to L_0, but with no long-range ordering observed in the BCP films. A similar result was obtained for the other two cases when $L_s \approx \sqrt{3}L_0$ (Figure 7i−m) and when $L_s \approx 2L_0$ (Figure 7n−r).

A simple free-energy model was introduced to predict the possible configuration(s) with different L_s for sphere-forming P(S-*b*-DMS) on a topography prepattern.[19] According to this model, there is an energy well for forming each BCP pattern lattice configuration <*i j*> when $L_s/L_0 = \sqrt{(i^2 + j^2 + ij)}$ and configuration <*i j*> dominates the BCP pattern with $L_p = L_0$. If the prepattern is not commensurate with equilibrant BCP pattern lattice, more than one lattice configuration will appear in the BCP films. For instance, two lattice configurations of <2 0> and <2 1> were observed simultaneously even when the ratio of L_s/L_0 is only slightly larger than 2.[19] This will introduce defects into the BCP pattern and is certainly a drawback for the BPM applications that prefer only one perfect lattice structure shows up in the data bit area. Here cylinder-forming P(S-*b*-MMA) with L_0 of 28.6 nm is directly self-assembled on prepatterns with a surface pattern period ranging from 46 nm ($1.6L_0$) $\leq L_s \leq$ 62 nm ($2.2L_0$). According to the free-energy model, both lattice configurations <1 1> and <2 0> are expected to be observed when 49.5 nm ($\sqrt{3}L_0$) $< L_s <$ 57.2 nm ($2L_0$). Similarly, lattice configuration <2 0> will coexist with lattice configuration <2 1> for the case of 57.2 nm ($2L_0$) $< L_s <$ 75.7 nm ($\sqrt{7}L_0$). However, we observed the BCP patterns with nearly 100% <1 1> lattice configuration for the case of $L_s = 48$, 50, and 52 nm and with a dominant <2 0> lattice configuration for $L_s = 56$, 58, and 60 nm. The reason for observing only one lattice structure instead of two (or more) in both cases is because the limitation of the dimensional commensurability rules out one of the two lattice structures. To explain this more clearly, Table 1 lists the calculated BCP pattern pitches L_p, based on a $L_0 = 28.6$ nm BCP, for the three different lattice configurations <1 1>, <2 0>, and <2 1> in the BCP films that were directed by prepatterns with different L_s ranging from 46 to 62 nm, in steps of 2 nm. For instance, when $L_s = 60$ nm, L_p will be 34.6 nm if the BCP pattern is a <1 1> lattice configuration, 30.0 nm for

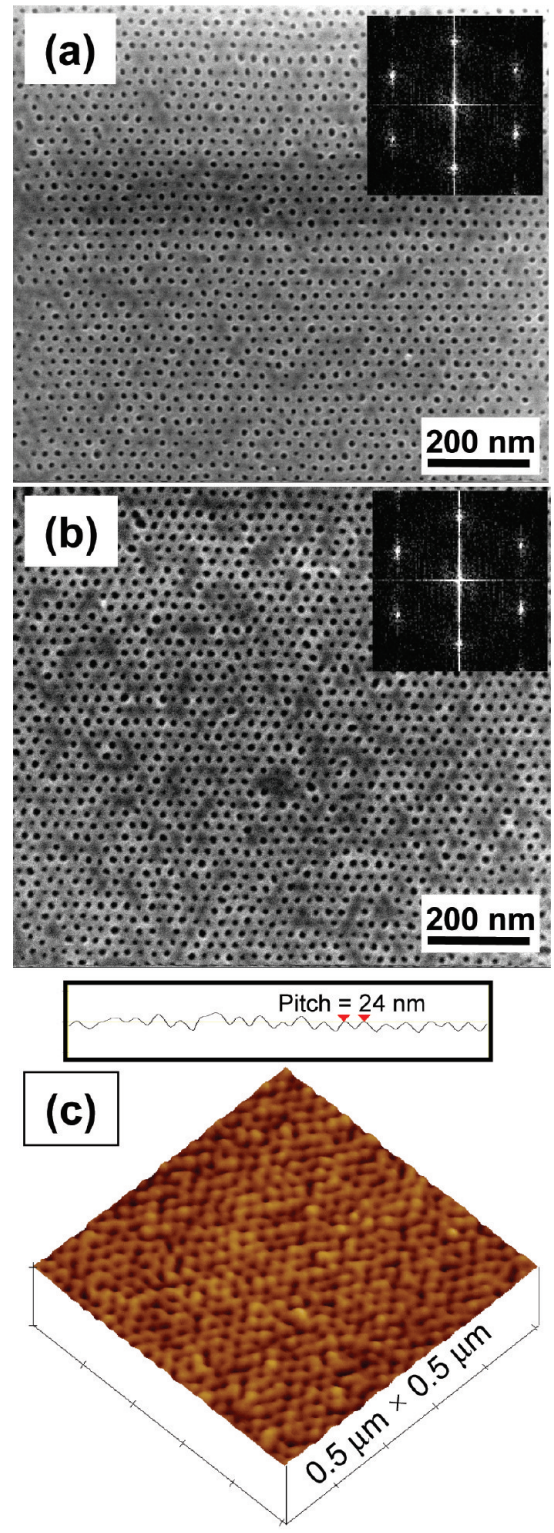

Figure 8. SEM images of P(S-*b*-MMA) ($L_0 = 24$ nm, 1.3 Tb/in.^{2}) on prepatterns with (a) $L_s = 24$ nm and (b) $L_s = 48$ nm. (c) AFM height image of P(S-*b*-MMA) pattern on prepattern with $L_s = 48$ nm. *Z* range is 5.0 nm.

<2 0> lattice configuration, and 22.7 nm for <2 1> lattice configuration. Patterns with these three lattice configurations can possibly form in the BCP films according to the free-energy model. However, our experimental results show that the cylinder-forming P(S-*b*-MMA) with L_0 of 28.6 nm can neither compress its pitch lower than 27 nm nor stretch to a pitch beyond 30 nm. Thus only the <2 0> lattice configuration is observed in the BCP pattern on a prepattern with L_s = 60 nm, and the other two lattice configurations were restricted and so were not observed in the present experiment. In Table 1, all of the calculated L_p values that are beyond the dimensional latitude range are marked in red, and all of the L_p values that are within the dimensional latitude range are marked in green. The two L_p values marked yellow represent that the value is close to edge of the dimensional latitude range. Clearly, prepatterns with a L_s of 48, 50, or 52 nm can only guide BCP patterns to form a <1 1> lattice configuration. The BCP pattern pitches measured from our experiments are very close to the calculated L_p values in Table 1, which represent the BCP chain either compressing or stretching to comply to the surface prepattern L_s value. Similarly, only the <2 0> lattice configuration was observed for the case of L_s = 56, 58, and 60 nm. When BCP patterns with a <1 1> lattice configuration form on prepatterns with a L_s of 52 nm, or when a <2 0> lattice configuration forms on prepatterns with a L_s of 60 nm, we observed that both BCP patterns show similar pattern quality in the films that were directed on prepatterns with a L_s of 30 nm since the calculated L_p values are also approximately 30 nm for both cases. From Table 1, we can also see that when the BCP films are directed on prepatterns with a L_s of 46, 54, or 62 nm, all of the calculated L_p values are marked in red as an indication that all of those three columns of L_p values are beyond the dimensional latitude, resulting in the fact that prepatterns should not be able to guide the BCP films to form any single lattice configuration. Our experimental results confirm the calculated results mentioned above. In addition, the commensurability between the BCP lattice and the prepattern lattice was also studied in an extended range of $1.5L_0 \leq L_s \leq 2.4L_0$. We still did not observe the coexistence of more than one lattice configuration in BCP patterns as predicted in the theory. We believe this is due to the restriction of the dimensional latitude range of this BCP; some lattice configurations were restricted and since only one lattice configuration is possible while L_s is within the range of $\sim(1 \pm 0.05)\sqrt{(i^2 + j^2 + ij)}L_0$. By calculation, this rule would be correct for $\sqrt{(i^2 + j^2 + ij)} \leq 3$ if the density multiplication were possible. Multiple lattice configurations were expected to coexist while $\sqrt{(i^2 + j^2 + ij)} \geq \sqrt{12}$ ($i = j = 2$). When $L_s = \sqrt{12}L_0$, <3 1> configuration can form with $L_p = 0.96L_0$ besides the most stable configuration <2 2>.

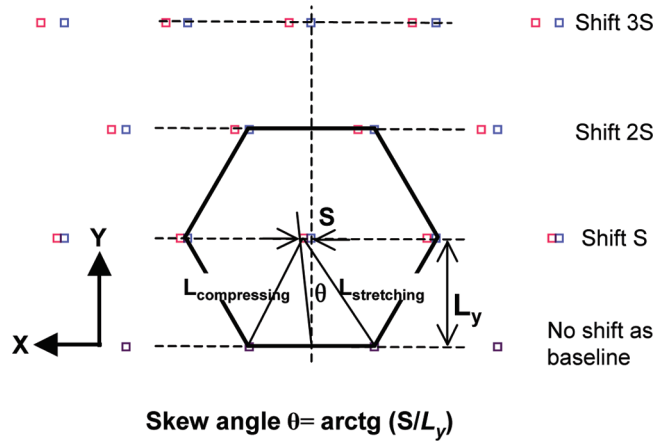

Figure 9. Drawing of a hexagonal pattern with a skew angle of θ. The blue squares denote a hexagon pattern with no skew, and the red squares denote a hexagon pattern with a skew angle θ. Every red square in a given row shifts in the *x*-direction by the amount *S* (nm) relative to its neighbor row to form a skewed hexagonal pattern. The skew angle can be calculated as θ = arctg(S/L_y).

In our experiment, low molecular weight P(S-*b*-MMA) with a L_0 = 24 nm (corresponding to a pattern density of 1.3 Tb/in.^{2}) was also investigated in order to push the pattern density beyond 1 Tb/in.^{2}. These samples were also prepared on a chemically patterned PS brush substrate, and with two pitch ranges from (1) $L_s \approx L_0$, 22 nm $\leq L_s \leq$ 25 nm and (2) $L_s \approx 2L_0$, 44 nm $\leq L_s \leq$ 50 nm. Long-range-ordered hexagonal BCP patterns were only observed for the cases when L_s = 24 and 48 nm. Figure 8 shows a top-down SEM image of a ~30 nm thick P(S-*b*-MMA) film with a L_0 = 24 nm on prepatterns with L_s = 24 nm shown in Figure 8a and L_s= 48 nm shown in Figure 8b. The P(S-*b*-MMA) exhibited an ordered hexagonal BCP pattern as shown in the inserted 2D fast Fourier transforms (FFT) in Figure 8a,b. However, more short-range defects were observed in the images than those assembled with a L_0 = 42 nm BCP (shown in Figure 3d−f and Figure 6b−e) or L_0= 28.6 nm BCP materials (shown in Figure 2f,g and Figure 5b). Some of the cylindrical pores did not fully open and formed a meandering pattern on the surface. AFM imaging was performed to image the surface roughness and topography of the BCP patterns. The AFM image (Figure 8c) shows the surface of the BCP pattern is smooth with a surface roughness rms of approximately 1.25 nm over a 500 nm × 500 nm scanning area. Some defective areas observed in the SEM images (the dark areas in Figure 8a,b) were also monitored by AFM (Figure 8c). These areas represent non-open holes and show similar thickness to the remaining BCP film. In the weak segregation limit theory, BCP can form the ordered domains as long as χN is greater than 10.5 for lamellar structures with a volume fraction of one block being 0.5;[27,28] χ is its Flory−Huggins interaction parameter, and N is the overall degree of polymerization. This χN minimum is larger than 10.5 for a cylinder-forming BCP based on the phase diagram; χN is only

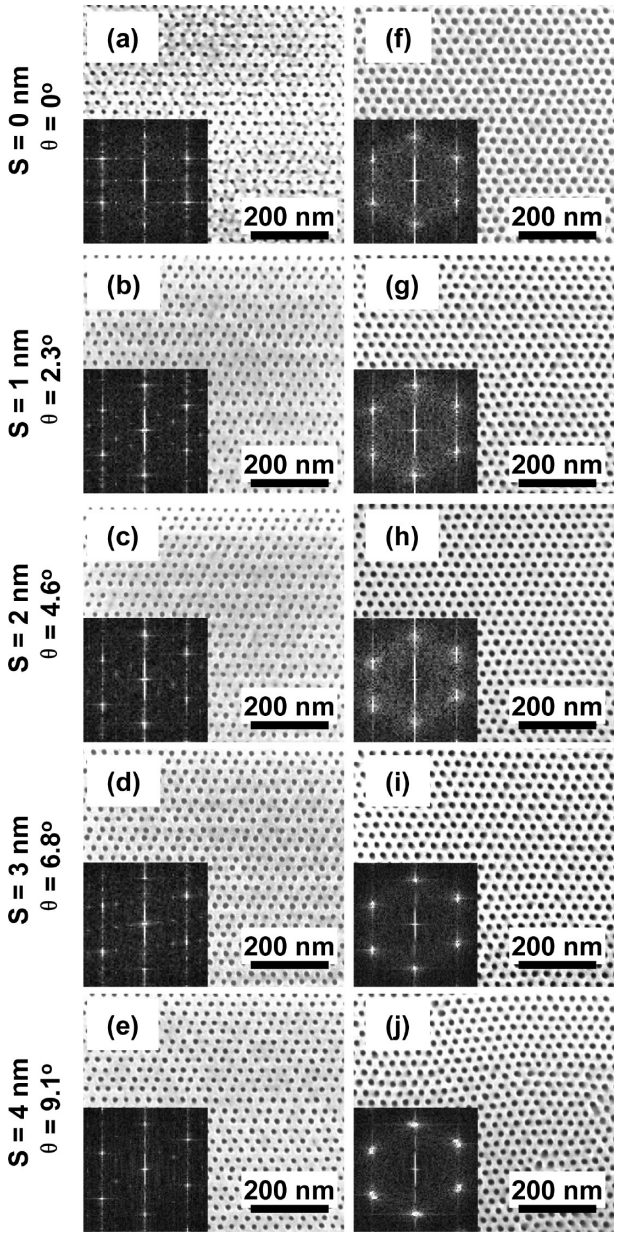

Figure 10. (a−e) SEM images of the e-beam resist patterns (L_s = 28 nm) with skew angles of 0, 2.3, 4.6, 6.8, and 9.1°, respectively. (f−j) SEM images of P(S-*b*-MMA) (L_0 = 28.6 nm) patterns directed by prepatterns with features corresponding to the e-beam resist patterns shown in (a−e), respectively. The insets show the 2D FFT graphs.

22.8 for cylinder-forming P(S-*b*-MMA) with a L_0 = 24 nm, which is very close to the minimum value required for the formation of well-ordered structures. Better BCP patterns at this density may be achievable by further optimizing the process conditions with the present prepattern system or by using a different prepattern approach that has a stronger chemical affinity than the current system; however, it is still very challenging to get the defect-free cylinder patterns in P(S-*b*-MMA) at this density of 1Tb/in.^{2} due to its small χ value of 0.06.[29] Different BCP materials that have a higher χ value are desirable for higher density patterning beyond 1 Tb/in.^{2}. BCP films with higher χ values have been reported, for instance, P(S-*b*-DMS) with a χ value of ~0.26.[30] With such high χ value BCP materials, the experimental results already indicate that BCP can be guided to achieve a pattern density up to ~4 Tb/in.^{2}.[2,31]

When the chemically patterned PS brush is used as prepattern, the dimensional latitudes are $\sim\pm14\%L_0$ for a ternary P(S-*b*-MMA)/PS/PMMA blend (forming lamella structure with L_0 = 70 nm)[10] and $\sim\pm10\%L_0$ for a lamella P(S-*b*-MMA) with L_0 = 47.5 nm,[25,32] respectively. For the first time, we studied the dimensional elastic compliance for cylinder-forming P(S-*b*-MMA)s with three molecular weights. It should be mentioned here that, limited by the pixel resolution in e-beam exposure tool, we can only prepare prepatterns with L_s in integer numbers with unit nanometer, which prevents us getting more precise pitch latitude results. However, our experimental results can still show that the dimensional range decreases with decreasing molecular weight. The dimensional latitude range is $\sim-5\%L_0$ to $+9.5\%L_0$ for P(S-*b*-MMA) with L_0 = 42 nm, $<\pm5\%L_0$ for P(S-*b*-MMA) with L_0 = 28.6 nm, and $<\pm4\%L_0$ for P(S-*b*-MMA) with L_0 = 24 nm, respectively. The change in free energy per chain of the BCP films can be simplified as $\Delta F = \Delta F_{interfacial} + \Delta F_{straining}$, where the $\Delta F_{interfacial}$ is the free energy to induce the self-assembly on the prepattern and the $\Delta F_{straining}$ is the change of free energy associated with deviations in L_p with respect to L_0. $\Delta F_{straining}$ has a minimum value zero when $L_s = L_0$, and it increases with L_s deviating to L_0, which is similar to the results predicted for the lamella-forming P(S-*b*-MMA).[33] $\Delta F_{interfacial}$ is usually negative and proportional to the molecular weight. The absolute value of $\Delta F_{interfacial}$ will decrease with molecular weight and will get close to the minimum of $\Delta F_{straining}$, which results in narrower dimensional latitude.

Directed Assembly on Skewed Hexagonal Prepatterns. It would be interesting to see if the BCP can still be guided on a hexagonal prepattern but with adding a small skew angle. This experiment has a practical meaning for BPM applications because the current mechanical design of hard disk drives requires a skew angle of approximately 15°. The dimensional latitude range, in the BCP films, directly determines how much the BCP pattern can be skewed. Figure 9 shows a drawing of a hexagonal pattern with a skew angle of θ that was used for determining the maximum skew angle in the BCP pattern. The blue squares in the drawing denote a hexagon pattern with no skew, whereas the red squares denote a hexagon pattern with a skew angle θ. Every red square in a given row shifts in the *x*-direction by the amount *S* (nm) relative to its neighbor row to form a skewed hexagonal pattern. The skew angle can be calculated as $\theta = \text{arctg}(S/L_y)$. On a skewed hexagon prepattern, the polymer chains need to stretch and compress simultaneously. Figure 10a−e shows top-down SEM images of e-beam resist with hexagonal patterns (L_s = 28 nm) and with skew angles of 0, 2.3, 4.6, 6.8, and

9.1°, respectively. Figure 10f−j shows top-town SEM images of BCP patterns directed by prepatterns with features corresponding to the e-beam patterns shown in Figure 10a−e. The inseted 2D FFT graphs serve as a good indication of the lattice configurations. Hexagonal patterns with no skew angle give a symmetric hexagonal pattern in the FFT graph, whereas a skewed pattern will result in an asymmetric hexagonal pattern in the FFT graph. As a result, we observed that the BCP patterns could perfectly follow the skewed underlying prepatterns up to a maximum of 6.8°. Above this skew angle, the BCP pattern could not follow the prepattern, resulting in the loss of long-range ordering as shown in Figure 10j. This can clearly be seen in the 2D FFT graph in Figure 10j, which shows relatively broad peaks compared to the 2D FFT graph in Figure 10e. Very similar results (with skew angles of up to approximately 7.0°) were obtained on skewed patterns in the case when $L_p = 28$ nm and $L_s = 56$ nm (Figure 11). More than one lattice configuration was observed when the skew angle was higher than approximately 7.0° with the current P(S-*b*-MMA) and PS brush prepattern system. A different BCP or prepattern system could produce a different maximum skew angle. When the skew angle is 7.0°, the stretched length ($L_{stretching}$) is approximately $1.05L_0$, and the compressed length ($L_{compressing}$) is approximately $0.977L_0$. Both lengths are still within the dimensional latitude range where nearly perfectly ordered BCP patterns can be achieved. When the skew angle is 9.3°, the $L_{stretching}$ of approximately $1.066L_0$ will exceed the maximum pitch dimensional latitude range, while the $L_{compressing}$ $0.962L_0$ is still in the range. The limitation of a maximum skew angle of 7.0° in the P(S-*b*-MMA) might not be sufficient to meet the current drive design, thus a modified P(S-*b*-MMA) or a new BCP system with a higher skew angle capability would be needed to accommodate today's hard disk drive architectures.

Non-Hexagonal Pre-Patterns for Directed Assembly. All commercially available cylinder-forming or sphere-forming BCP materials, such as P(S-*b*-MMA) or P(S-*b*-DMS), prefer to form a hexagonal lattice in the BCP film. It would be interesting to see if a BCP pattern can comply with a prepatterned substrate that has a non-hexagonal pattern. For this purpose, three non-hexagonal patterns including staggered, rectangular, and square lattice structures were used for the BCP process test. The SEM images show that the P(S-*b*-MMA) films with a $L_s = 42$ nm can still form ordered structures with a pitch of 42 nm for staggered patterns (Figure 12a), 42 nm × 39 nm for rectangular patterns (Figure 12b), and 42 nm for square patterns (Figure 12c); however, this kind of ordering is only short-range ordering; it is typically observed on several hundred square nanometers in area only, and there is no long-range ordering over a large area since the dimensions for all three patterns are out of the dimensional latitude range of $-5\%L_0$ to $+9.5\%L_0$

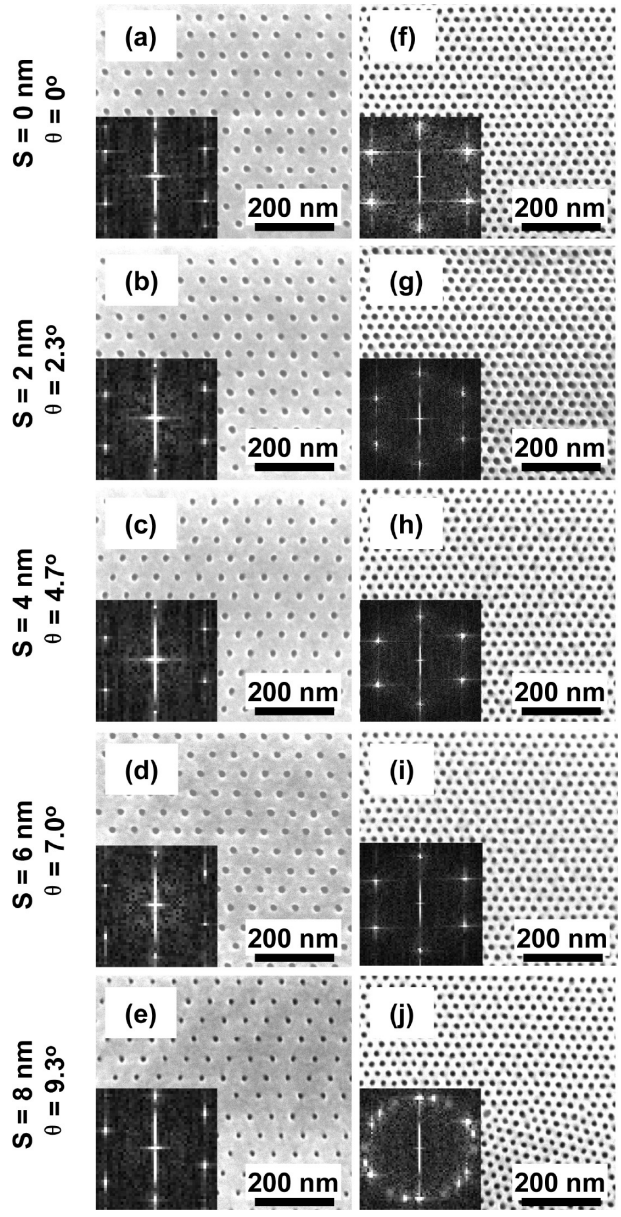

Figure 11. (a−e) SEM images of the e-beam resist patterns (L_s = 56 nm) with skew angles of 0, 2.3, 4.7, 7.0, and 9.3°, respectively. (f−j) SEM images of P(S-*b*-MMA) (L_0 = 28.6 nm) directed by prepatterns with features corresponding to the e-beam patterns shown in (a−e), respectively. The insets show the 2D FFT graphs.

for P(S-*b*-MMA) with $L_0 = 42$ nm. Among these three patterns, the staggered pattern falls on the edge of the dimensional latitude range while the other two patterns are far outside of the range. Long-range ordering not observed in these films, and many defects were observed in the BCP patterns, such as lying down cylinders, missing cylinders, and connected cylinders for the rectangular and square P(S-*b*-MMA) patterns because of the incommensurability between L_0 and the diagonal lattice spacing (57 nm for the rectangular and 59 nm for the square).[24] As shown in Figure 12a−c, the patterns in the BCP films are becoming more deformed as the prepattern moves from the staggered shape (Figure 12a) to the square shape (Figure 12c) because the poly-

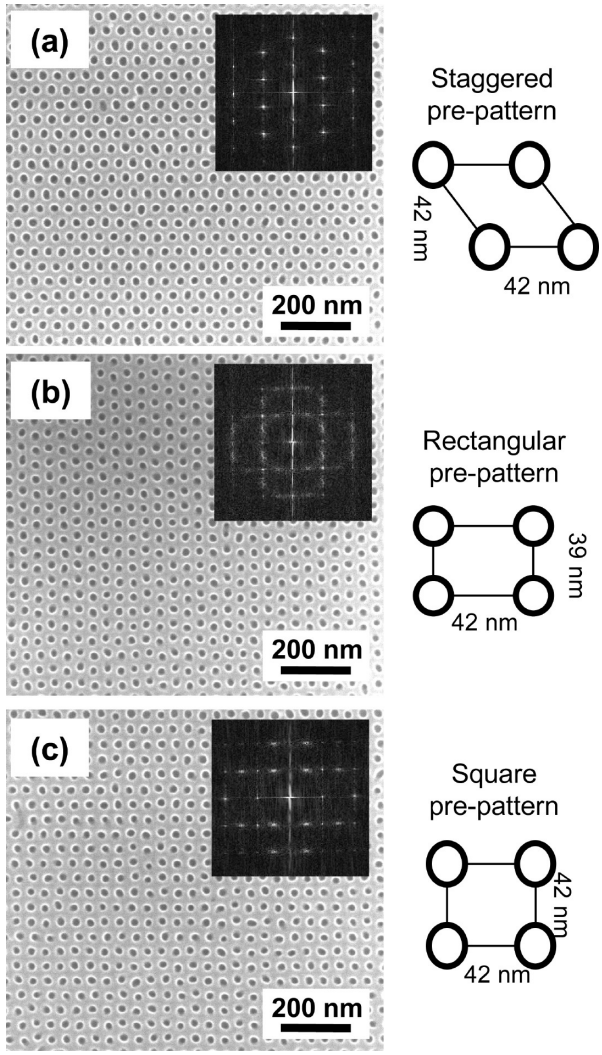

Figure 12. SEM images of P(S-*b*-MMA) (L_0 = 42 nm) patterns directed by non-hexagonal prepatterns: (a) staggered pattern with L_s = 42 nm, (b) 42 nm × 39 nm rectangular pattern, and (c) 42 nm × 42 nm square pattern. The insets show the 2D FFT graphs.

mer chains were over stressed trying to follow the prepattern, which was not a hexagonal pattern. Defect-free non-hexagonal lattice structures require the synthesis of a new BCP architecture to form a non-hexagonal lattice configuration. For instance, a highly ordered square array at the 20 nm scale with long-range ordering has been reported recently by combining polymer self-assembly of H-bonding units with controlled microphase separation of well-defined BCP.[34]

Challenges in BCP Approach for BPM. Several advantages of the BCP approach over the conventional e-beam process have been experimentally demonstrated in terms of the pattern quality, resolution, and process latitude. A nearly perfect hexagonal BCP pattern with long-range ordering and registration has been demonstrated at a pattern density of approximately 1 Tb/in.^{2}. It has also been mentioned above that higher densities beyond 1 Tb/in.^{2} are achievable by using other BCP materials with higher χ values.[31] However, for real BPM applications, the BCP approach still has several of its own challenges at the present early stage. Several challenges are briefly discussed here. First, the equilibrium structure for all commonly used BCP materials has a hexagonal lattice that may not provide the best topology for BPM applications. Any non-hexagonal structure requires the synthesis of a copolymer with new architecture to form a non-hexagonal pattern. Second, the maximum skew angle of less than 10° in the most BCP materials including P(S-*b*-MMA) may be another practical issue to limit this application or require the change of the current mechanical design to accommodate this low skew angle. The skew angle may be increased by adding a blend of polymer into the BCP to increase the dimensional latitude of the polymer chains,[10] but it comes at the risk of inducing more than one lattice configuration in the BCP pattern, which is not desirable for BPM applications. Third, since the BCP patterns only exhibit one lattice structure with a fixed dimension (pitch), that is suitable for forming the data bit area but may not be suitable for the servo pattern area that consists of periodic and nonperiodic structures with different dimensions. Due to the flexibility of the conventional e-beam lithography process, it can more easily handle the servo pattern area than the BCP process. Therefore, the practical solution will be to integrate two processes into one template fabrication process by using the BCP process for the data bit area and using the conventional e-beam process for the servo pattern area. Then how to integrate these two processes along with tight overlay requirements becomes the next challenge.

CONCLUSIONS

In conclusion, this work demonstrated that a nearly perfect hexagonal BCP pattern with long-range ordering and registration can be achieved at a density of approximately 1 Tb/in.^{2} using a cylinder-forming P(S-*b*-MMA) system. The σ value in the BCP process has significantly decreased by approximately 2.3% for size variation and approximately 4−5% for the placement accuracy with respect to the e-beam prepatterns. The BCP process shows an exposure dosage range approximately four times wider than that of e-beam resist process. The maximum dimensional latitude, where the BCP pattern can either stretch or compress, decreases with the decrease in the BCP molecular weight, and the latitude value is sensitive to thermal annealing conditions in the BCP process. When the prepattern period L_s ranges from 1.5L_0 to 2.4L_0, BCP patterns with L_0 of 28.6 nm are observed with only one lattice configuration because the narrow dimensional latitude restricts the formation of other lattice configurations. The P(S-*b*-MMA) patterns can follow a skewed hexagonal prepattern and still maintain long-range ordering up to approximately 7° (skew angle) without significant defects. More defects in the BCP patterns were observed in the following two cases: (1) in low molecular weight P(S-*b*-MMA)

with a $L_0 = 24$ nm because the χN, in this case, is very close to the minimum value required for the formation of well-ordered cylindrical structures, and (2) on non-hexagonal prepatterns due to the dimensional latitude restriction. Finally, several limitations and challenges in the BCP approach that are associated with BPM applications have been mentioned. These challenges will be further explored in our future study.

EXPERIMENTAL SECTION

Materials. Polished 150 mm diameter Si⟨100⟩ wafers with a 300 nm thick thermal oxide layer were purchased from Silicon Quest Int'l and used as substrates for the deposition of films. All block copolymers were purchased from Polymer Source Inc. P(S-*b*-MMA)s with three different molecular weights were used in our experiments: (1) number-average molar mass, $M_n = 67.1$ kg/mol (corresponding to bulk equilibrium cylinder period, $L_0 = 42.0$ nm), polydispersity (PDI) = 1.09, styrene block volume fraction = 0.70; (2) $M_n = 53.8$ kg/mol ($L_0 = 28.6$ nm), PDI = 1.07, styrene block volume fraction = 0.70; and (3) $M_n = 39$ kg/mol ($L_0 = 24.0$ nm), PDI = 1.07, styrene block volume fraction = 0.70. The monohydroxyl-terminated polystyrene (PS−OH), M_n of 3.7 kg/mol, was used as the chemical prepatterning layer to modify the SiO_2 surface. The e-beam resist ZEP520 was purchased from Nippon Zeon and was used for producing the prepatterns. All other chemicals were purchased from Sigma-Aldrich.

Sample Preparation. The directed self-assembly process is described as follows: (1) Prepare oxidized silicon wafers with the polystyrene brush treatment. The SiO_2 substrates are precleaned using O_2 plasma ashing at 100 °C for 5 min and spin-coated with PS−OH, and then annealed at 165 °C for ~12 h under vacuum. The wafers were then soaked in toluene for 15 min and rinsed with isopropanol (IPA) and blown dry with N_2. The grafted PS thickness is 2−3 nm. (2) E-beam patterning: The exposure was performed using a Vistec VB6 HR direct write vector beam lithography system operating at 100 keV. Maximum write speed is 25.5 MHz operating at a beam current range of 0.3−1.0 nA. CAD data were transposed into Vistec format with CATS software from Transcription Enterprises. A ~45 nm thick ZEP520 e-beam resist was spin-coated and baked at 180 °C for 5 min and e-beam exposed at the dose of 20−200 mC/cm^2. The developer for the ZEP resist is IPA, and the wafer is developed for 15 s with ultrasonic energy then rinsed in DI water for 30 s. (3) Surface treatment and resist strip: The patterned substrate is then etched by O_2 RIE at 100 W for 3−5 s in order to remove the ZEP520 residue and also remove the PS brush layer in the patterned areas. A chemical contrast dot prepattern (SiO_2 exposed dot areas surrounded by a PS brush matrix) is formed on the substrate. After that, the ZEP520 resist was stripped by soaking in EBR (2-(1-methoxy)propyl acetate (PGMEA) solution) at 60 °C for 1 h and sonicated for 20 min and then blown dry with N_2. (4) Preparation of the BCP film: Thin P(S-*b*-MMA) films were spin-coated with film the thickness ranging from 30 to 60 nm and annealed in a vacuum oven at a temperature range of 170−220 °C for 2−24 h. The PMMA blocks are removed by flood exposing the substrate to deep ultraviolet (DUV) for ~10 min and soaking in acetic acid for ~1 min.

Metrology Characterization. The resist and BCP film thickness are determined using a KLA-Tencor profilometer. AFM measurements are performed in the tapping mode with a Dimension 5000 system (Veeco Digital Instruments). Scanning electron microscopy (SEM) characterization was conducted using a NOVA SEM system (FEI). The resist patterns are over coated with a 1 nm thick tantalum layer to dissipate charging before SEM imaging.

Image Analysis for σ Calculation. The size distribution and position accuracy analysis was performed based on high-quality SEM images and commercial software purchased from Simagis. SEM images were taken on random patterned areas from different samples. The same magnification (250 or 350K×) was used for a series of images. The dot diameter is defined as a diameter of a circle, either inscribed within the dot or circumscribed around the dots' external contour. The size σ of the dot is defined as a quotient of the standard deviation of the dot diameter divided by the dot diameter. The center of each dot is extracted for positional σ analysis. The *x*-direction is defined along the <1 0> direction of the hexagonal pattern which is the e-beam raster scanning direction of the VB6 vector beam tool. The e-beam raster scanning direction is defined as the *x*-direction (*x*-axis), and the *y*-direction is defined as being perpendicular to the *x*-direction. After setting several parameters, in the software, the dot-to-dot distance along the axis, the interaxis distance, and the dot-to-axis distance and their standard deviation are then calculated by the software. Positional σ along the *x*-direction (σ_x) is defined as a quotient of the standard deviation of the dot-to-dot distance along the *x*-axis divided by the dot-to-dot distance along the *x*-axis. Positional σ along the *y*-direction (σ_y) is defined as $\sigma_y = \sqrt{(\sigma_{y1}^2 + \sigma_{y2}^2)}$ where σ_{y1} is the quotient of standard deviation of the dot-to-axis distance divided by the dot-to-axis distance and σ_{y2} is a quotient of the standard deviation of the interaxis distance divided by the interaxis distance. It should be mentioned that the σ values are highly dependent on image quality, parameter setup, and the algorithm. Therefore, the calculated σ number can be quite different. The absolute number is less important than the relative number because the σ values obtained here are used only for the purpose of evaluating the process.

Acknowledgment. The authors would like to thank Seagate Research Team, especially K. Mountfield for the computer-aided design (CAD) work and C. Seiler for experimental support.

REFERENCES AND NOTES

1. White, R. L.; Newt, R. M. H.; Pease, R. F. W. Patterned Media: A Viable Route to 50 Gbit/in^2 and up for Magnetic Recording. *Magn. IEEE Trans.* **1997**, *33*, 990–995.
2. Hughes, G. Patterned Media. In *Physics of Magnetic Recording*; Springer: Berlin, 2001.
3. Richter, H. J.; Dobin, A. Y.; Lynch, R. T.; Weller, D.; Brockie, R. M.; Heinonen, O.; Gao, K. Z.; Xue, J.; Van der Veerdonk, R. J. M.; Asselin, P.; Erden, M. F. Recording Potential of Bit-Patterned Media. *Appl. Phys. Lett.* **2006**, *88*, 222512.
4. International Technology Roadmap for Semiconductors, http://www.itrs.net/Links/2007ITRS/Home2007.htm.
5. Resnick, D. J.; Sreenivasan, S. V.; Willson, C. G. Step & Flash Imprint Lithography. *Mater. Today* **2005**, *8*, 34–42.
6. Yang, X. M.; Xiao, S.; Wu, W.; Xu, Y.; Mountfield, K.; Rottmayer, R.; Lee, K.; Kuo, D.; Weller, D. Challenges in 1 Teradot/in.^{2} Dot Patterning Using Electron Beam Lithography for Bit-Patterned Media. *J. Vac. Sci. Technol., B* **2007**, *25*, 2202–2209.
7. Yang, X. M.; Xu, Y.; Seiler, C.; Wan, L.; Xiao, S. Toward 1 Tdot/in.^{2} Nanoimprint Lithography for Magnetic Bit-Patterned Media: Opportunities and Challenges. *J. Vac. Sci. Technol., B* **2008**, *26*, 2604–2610.
8. Rockford, L.; Liu, Y.; Mansky, P.; Russell, T. P.; Yoon, M.; Mochrie, S. G. J. Polymers on Nanoperiodic, Heterogeneous Surfaces. *Phys. Rev. Lett.* **1999**, *82*, 2602.
9. Ouk Kim, S.; Solak, H. H.; Stoykovich, M. P.; Ferrier, N. J.; de Pablo, J. J.; Nealey, P. F. Epitaxial Self-Assembly of Block Copolymers on Lithographically Defined Nanopatterned Substrates. *Nature* **2003**, *424*, 411–414.
10. Stoykovich, M. P.; Muller, M.; Kim, S. O.; Solak, H. H.; Edwards, E. W.; de Pablo, J. J.; Nealey, P. F. Directed Assembly of Block Copolymer Blends into Nonregular Device-Oriented Structures. *Science* **2005**, *308*, 1442–1446.
11. Segalman, R. A.; Yokoyama, H.; Kramer, E. J. Graphoepitaxy of Spherical Domain Block Copolymer Films. *Adv. Mater.* **2001**, *13*, 1152–1155.

12. Cheng, J. Y.; Ross, C. A.; Thomas, E. L.; Smith, H. I.; Vancso, G. J. Fabrication of Nanostructures with Long-Range Order Using Block Copolymer Lithography. *Appl. Phys. Lett.* **2002**, *81*, 3657–3659.
13. Park, S.; Kim, B.; Yavuzcetin, O.; Tuominen, M. T.; Russell, T. P. Ordering of PS-*b*-P4 VP on Patterned Silicon Surfaces. *ACS Nano* **2008**, *2*, 1363–1370.
14. Cheng, J. Y.; Ross, C. A.; Smith, H. I.; Thomas, E. L. Templated Self-Assembly of Block Copolymers: Top-Down Helps Bottom-Up. *Adv. Mater.* **2006**, *18*, 2505–2521.
15. Darling, S. B. Directing the Self-Assembly of Block Copolymers. *Prog. Polym. Sci.* **2007**, *32*, 1152–1204.
16. Yang, X. M.; Peters, R. D.; Kim, T. K.; Nealey, P. F. Patterning of Self-Assembled Monolayers with Lateral Dimensions of 0.15 μm Using Advanced Lithography. *J. Vac. Sci. Technol., B* **1999**, *17*, 3203–3207.
17. Yang, X. M.; Peters, R. D.; Nealey, P. F.; Solak, H. H.; Cerrina, F. Guided Self-Assembly of Symmetric Diblock Copolymer Films on Chemically Nanopatterned Substrates. *Macromolecules* **2000**, *33*, 9575–9582.
18. Ruiz, R.; Kang, H.; Detcheverry, F. A.; Dobisz, E.; Kercher, D. S.; Albrecht, T. R.; de Pablo, J. J.; Nealey, P. F. Density Multiplication and Improved Lithography by Directed Block Copolymer Assembly. *Science* **2008**, *321*, 936–939.
19. Bita, I.; Yang, J. K. W.; Jung, Y. S.; Ross, C. A.; Thomas, E. L.; Berggren, K. K. Graphoepitaxy of Self-Assembled Block Copolymers on Two-Dimensional Periodic Patterned Templates. *Science* **2008**, *321*, 939–943.
20. Cheng, J. Y.; Rettner, C. T.; Sanders, D. P.; Kim, H.-C.; Hinsberg, W. D. Dense Self-Assembly on Sparse Chemical Patterns: Rectifying and Multiplying Lithographic Patterns Using Block Copolymers. *Adv. Mater.* **2008**, *20*, 3155–3158.
21. Edwards, E. W.; Muller, M.; Stoykovich, M. P.; Solak, H. H.; dePablo, J. J.; Nealey, P. F. Dimensions and Shapes of Block Copolymer Domains Assembled on Lithographically Defined Chemically Patterned Substrates. *Macromolecules* **2007**, *40*, 90–96.
22. Burger, C.; Ruland, W.; Semenov, A. N. Polydispersity Effects on the Microphase-Separation Transition in Block Copolymers. *Macromolecules* **1990**, *23*, 3339–3346.
23. Scott, W. S.; Glenn, H. F. Continuous Polydispersity in a Self-Consistent Field Theory for Diblock Copolymers. *J. Chem. Phys.* **2004**, *121*, 4974–4986.
24. Park, S.-M.; Craig, G. S. W.; La, Y.-H.; Solak, H. H.; Nealey, P. F. Square Arrays of Vertical Cylinders of PS-*b*-PMMA on Chemically Nanopatterned Surfaces. *Macromolecules* **2007**, *40*, 5084–5094.
25. Edwards, E. W.; Montague, M. F.; Solak, H. H.; Hawker, C. J.; Nealey, P. F. Precise Control over Molecular Dimensions of Block-Copolymer Domains Using the Interfacial Energy of Chemically Nanopatterned Substrates. *Adv. Mater.* **2004**, *16*, 1315–1319.
26. Wang, Q.; Nealey, P. F.; de Pablo, J. J. Monte Carlo Simulations of Asymmetric Diblock Copolymer Thin Films Confined between Two Homogeneous Surfaces. *Macromolecules* **2001**, *34*, 3458–3470.
27. Leibler, L. Theory of Microphase Separation in Block Copolymers. *Macromolecules* **1980**, *13*, 1602–1617.
28. Bates, F. S.; Fredrickson, G. H. Block Copolymer Thermodynamics: Theory and Experiment. *Annu. Rev. Phys. Chem.* **1990**, *41*, 525–557.
29. Russell, T. P.; Hjelm, R. P.; Seeger, P. A. Temperature Dependence of the Interaction Parameter of Polystyrene and Poly(methyl methacrylate). *Macromolecules* **1990**, *23*, 890–893.
30. Nose, T. Coexistence Curves of Polystyrene/Poly(dimethylsiloxane) Blends. *Polymer* **1995**, *36*, 2243–2248.
31. Xiao, S.; Yang, X. M.; Park, S.; Weller, D.; Russell, T. P., A General Approach to Addressable 4 Tdot/in^2 Pattered Media. *Adv. Mater.* **2009**, Early View.
32. Stoykovich, M. P.; Nealey, P. F. Block Copolymers and Conventional Lithography. *Mater. Today* **2006**, *9*, 20–29.
33. Wang, Q.; Nath, S. K.; Graham, M. D.; Nealey, P. F.; de Pablo, J. J. Symmetric Diblock Copolymer Thin Films Confined between Homogeneous and Patterned Surfaces: Simulations and Theory. *J. Chem. Phys.* **2000**, *112*, 9996–10010.
34. Tang, C.; Lennon, E. M.; Fredrickson, G. H.; Kramer, E. J.; Hawker, C. J. Evolution of Block Copolymer Lithography to Highly Ordered Square Arrays. *Science* **2008**, *322*, 429–432.